Materials Advances

ROYAL SOCIETY OF CHEMISTRY

PAPER

Published on 30 July 2026

Cite this: *Mater. Adv.*, 2026, 7, 8772

Electronic structure modulation *via* Mn(Ti) doping in epitaxial $SrTi_{1-x}Mn_xO_3$

M. Tyunina, *[ab] L. L. Rusevich, [c] E. de Prado, [b] N. Nepomniashchaia, [b] T. Kocourek, [b] A. E. Kotomin [cd] and A. Dejneka [b]

Received 6th June 2026,
Accepted 29th July 2026

DOI: 10.1039/d6ma00825a

rsc.li/materials-advances

Application-relevant properties of technologically important ABO_3-type perovskite oxides are primarily tailored through cationic substitution. Specifically, the electronic properties of the archetypal perovskite $SrTiO_3$ are modified by doping with transition metals such as Mn. However, the explicit role of the Mn cation remains elusive due to its multiple valence states, dual-site occupancy, and rich associated defect chemistry. In this study, the distinct impact of Mn substitution for Ti on the electronic structure of $SrTiO_3$ is established through combined theoretical and experimental investigations. First-principles calculations show that Mn(Ti) incorporation induces lattice contraction and introduces modifications to the conduction-band density of states, including band tailing and fine structure. To validate these predictions, a high-quality epitaxial film doped with 2 at.% Mn is grown on a contractive substrate that promotes contractive Mn(Ti) substitution. Optical studies of the doped film, benchmarked against both single-crystal and epitaxial $SrTiO_3$, reveal band tailing with in-gap depth of about 0.8 eV and the emergence of a near-edge transition—all consistent with theory.

Introduction

ABO_3-type perovskite oxides span the full spectrum of electronic behavior—from insulating to superconducting—and exhibit a wide variety of functional properties that enable applications across electronics, photonics, and catalysis. Among the most extensively studied archetypal perovskites, strontium titanate ($SrTiO_3$, STO) serves as an excellent platform for exploring the fundamental physics and chemistry of ABO_3 oxides. A key advantage of this class of materials is their ability to accommodate a broad range of cation substitutions while retaining phase stability. Such controlled doping is a well-established strategy for tailoring application-relevant properties. In STO, transition-metal doping—particularly with Mn—has been investigated for decades.[1–37] Early studies were primarily academic in nature,[1–4] followed by extensive work on the dielectric properties of Mn-doped STO (MSTO) for mainstream capacitor technologies.[5–26] More recently, motivated by seminal discoveries[27] and by contemporary energy and environmental challenges, significant effort has shifted toward STO-based photocatalysis, where Mn doping is employed to enhance visible-light absorption and to improve photocarrier generation and transport.[28–37] Precise understanding of how Mn influences the electronic properties of MSTO is therefore essential for advancing this field.

Mn cations can adopt multiple valence states ($Mn^{2+}/Mn^{3+}/Mn^{4+}$) and substitute on both the Ti site (denoted Mn(Ti)) and the Sr site (denoted Mn(Sr)) in STO.[10,11,21,23,25] Charge imbalance associated with Mn^{2+}/Mn^{3+} on the Ti^{4+} site or Mn^{3+} on the Sr^{2+} site can drive the formation of oxygen vacancies and defect complexes.[21,23] Because the preferred substitution site is often regulated by adjusting the Sr:Ti ratio, cation vacancies may also form. In addition, Mn can segregate to grain boundaries, occupy interstitial positions, or form Mn-rich aggregates.[13,16,17,21–24] This rich defect chemistry associated with synthesis of Mn doped STO ceramics and crystals gives rise to a wide range of electronic behaviors that are highly sensitive to synthesis conditions, often unpredictable, and not directly attributable to Mn alone. Such uncertainty complicates experimental efforts to isolate the intrinsic Mn-induced electronic properties. In this work, we overcome these challenges using an epitaxial thin-film approach.

Epitaxial growth enables the fabrication of high-quality, single-crystal-like materials with exceptional structural perfection. Unlike bulk crystals or ceramics, epitaxial films can be produced with minimal defects, a characteristic that underpins the success of modern microelectronics. After nearly three decades of intensive research, the reproducible growth of high-quality epitaxial STO films is now well established. Extensive studies have clarified

[a] *Microelectronics Research Unit, Faculty of Information Technology and Electrical Engineering, University of Oulu, P. O. Box 4500, FI-90014 Oulu, Finland. E-mail: marina.tjunina@oulu.fi*
[b] *Institute of Physics of the Czech Academy of Sciences, Na Slovance 2, 18221 Prague, Czech Republic*
[c] *Institute of Solid State Physics, University of Latvia, Kengaraga Str. 8, LV-1063 Riga, Latvia*
[d] *Max Planck Institute for Solid State Research, Heisenberg Str. 1, Stuttgart D-70569, Germany*

how substrate-induced lattice distortions influence the growth behaviour, crystal phases, and functional properties of epitaxial STO. Moreover, compared with crystal or ceramic synthesis, thin-film growth by pulsed laser deposition offers high oxygen pressure, low temperature, and short synthesis duration, conditions that suppress the formation of defect complexes and Mn aggregates. The absence of grain boundaries in high-quality epitaxial films provides an additional advantage.

Notably, substitutions and structural defects generally cause lattice deformations, either expansion (dilation) or shrinkage (contraction), and are thus dilative or contractive defects, correspondingly. Concurrently, in epitaxial films, lattice deformations arise from film–substrate mismatch, quantified as the misfit strain. Substrates with lattice parameters larger (smaller) than those of unstressed free film material impose in-plane tensile (compressive) strain and can therefore be considered dilative (contractive) in direct analogy to defect-induced lattice distortions. Because the elastic energy, stored in an epitaxial film, scales with the square of the misfit strain, the formation of defects that partially relieve this strain becomes energetically favourable. Consequently, dilative substrates tend to promote dilative defects, whereas contractive substrates favour contractive ones. In Mn-doped STO, Mn^{4+}(Ti) substitution is expected to be contractive, whereas other substitutions, vacancies, divacancies, and aggregates are dilative defects.[10,11,14,21,23,24,38]

In this work, we confirm lattice contraction around Mn^{4+}(Ti), demonstrating that a contractive substrate promotes such substitution in STO films. Prior studies have reported substrate-driven substitution for transition-metal dopants including Mn, Fe, Co, and Ni in epitaxial STO.[39,40] Well-established approaches for identifying substitutional sites typically rely on combining theoretical calculations with spectroscopic probes such as electron paramagnetic resonance, extended X-ray absorption fine structure, or X-ray absorption near-edge structure. These techniques, however, are not applicable to thin STO films because the thick insulating substrates required for epitaxy obscure the relevant signals.[23] In contrast, integrating theoretical calculations with analysis of epitaxial relationships and lattice strain provides a viable route for assessing contractive substitutions in thin films.

Substrate-induced strain increases the elastic energy of the film, and this energy grows with thickness. As a result, a critical thickness exists beyond which strain relaxation begins. Once relaxation occurs, the substrate's ability to dictate and stabilize specific substitution sites is reduced. Relaxation further produces a depth-dependent strain profile, yielding inhomogeneous strain across the film. Recent work shows that such inhomogeneous strain can induce tailing of electronic energy bands.[41] Indeed, ~150-nm-thick epitaxial STO films doped with Mn, Fe, Co, or Ni and grown on compressive substrates exhibit pronounced structurally driven optical band tailing.[39] Because structural tailing masks potential dopant-induced modifications of the band edges, eliminating inhomogeneous strain is essential for isolating the intrinsic electronic role of dopants. Achieving this condition requires reducing the thickness of epitaxial films.

In this work, we prepared a very thin, only 20 nm in thickness, epitaxial film of Mn-doped STO on a contractive substrate, thus ensuring dominating contractive Mn(Ti) substitution. By investigating the optical properties of the film in a broad spectral range, we identified Mn(Ti)-induced changes compared to pure STO crystal and strained film. We combined the experiments with the theoretical first-principles calculations. The obtained strong correspondence between calculated and measured signatures indicates that the main role of Mn(Ti) substitution in the electronic band structure is in a deep in-gap tailing at the bottom of the conduction band.

Methods

First-principles calculations

First-principles (*ab initio*) simulations were performed to investigate the effects of substitutional manganese (Mn) impurities in both unstrained and epitaxially compressed $SrTiO_3$ (STO). The structural and electronic properties of the material were studied within the framework of density functional theory (DFT) using the linear combination of atomic orbitals (LCAO) approach, as implemented in the CRYSTAL23 computer code.[42,43] Gaussian-type basis sets combined with the Hay–Wadt small-core effective core pseudopotential were employed for Sr and Ti atoms,[44] whereas all-electron basis sets were used for O and Mn atoms.[44,45] The B1WC global hybrid exchange–correlation functional was adopted throughout the calculations.[43] This combination of basis sets and functional has previously demonstrated high reliability in our simulations of STO-based systems.[46,47]

The calculations were performed for the low-temperature tetragonal phase of STO (space group SG 140, *I4/mcm*), whose crystallographic unit cell contains 20 atoms (4 Sr, 4 Ti, and 12 O). Full structural optimization was carried out, the band gap was evaluated, and the electronic density of states (DOS) was calculated. Six computational models were considered: (1) unstrained defect-free STO (free pure); (2) compressed defect-free STO (compressed pure); (3) unstrained STO with a Mn^{4+} substituting for Ti^{4+} (free Mn^{4+}(Ti)); (4) compressed STO with a Mn^{4+} substituting for Ti^{4+} (compressed Mn^{4+}(Ti)); (5) unstrained STO with a Mn^{2+} substituting for Sr^{2+} (free Mn^{2+}(Sr)); and (6) compressed STO with a Mn^{2+} substituting for Sr^{2+} (compressed Mn^{2+}(Sr)). Here, only isovalent substitutions were considered because defect complexes arising to compensate charge imbalance for $Mn^{2+}/Mn^{3+}(Ti^{4+})$ or $Mn^{3+}/Mn^{4+}(Sr^{2+})$ are dilative and unfavourable in epitaxial films on contractive substrates.

The Mn^{4+} ion has three unpaired electrons ($3d^3$), whereas the Mn^{2+} ion has five unpaired electrons ($3d^5$). Therefore, spin-polarized calculations were performed using the unrestricted open-shell DFT formalism.[43] The total spin of the Mn^{4+}(Ti) system was $S_z = 3/2$, whereas that of the Mn^{2+}(Sr) system was $S_z = 5/2$.

To simulate epitaxial compression, the lattice parameters ($a = b$) were reduced by 0.4% relative to those of pristine unstrained STO and subsequently kept fixed. The lattice parameter (c) and the atomic coordinates were fully relaxed during the geometry optimization. The defect-free system and the systems containing Mn^{4+}(Ti) defects were calculated in tetragonal

symmetry, whereas the systems containing Mn^{2+}(Sr) defects were treated without symmetry constraints (SG 1, *P1*). The defect concentration was 25%, corresponding to the substitution of one out of four Ti or Sr atoms by Mn.

Experimental

A thin (~20 nm) Mn-doped $SrTiO_3$ (MSTO, 2 at% Mn) film was grown by pulsed-laser deposition (PLD) at elevated temperature, under high ambient oxygen pressure, and using substrate scanning.[39,40,48–51] The deposition parameters were optimized to ensure proper films stoichiometry and uniformity: KrF excimer laser wavelength 248 nm, laser fluence 2 J cm^{-2}, substrate temperature 700 °C, and oxygen pressure 20 Pa. During post-deposition cooling, the oxygen pressure was gradually increased to 8×10^4 Pa at a rate of 5 °C min^{-1}. A single-crystal (001)-oriented $(LaAlO_3)_{0.3}(Sr_2AlTaO_6)_{0.7}$ (LSAT) substrate was used.

The crystal structure, phase purity, epitaxial quality, and lattice parameters of the film were examined by high-resolution X-ray diffraction (HRXRD) using a SmartLab SE multipurpose diffractometer (Rigaku Corp.) equipped with Cu $K\alpha_1$ radiation and a HyPix-3000 2D detector operated in 0D mode. The incident-beam optics consisted of a parabolic Göbel mirror, a two-bounce Ge(220) monochromator, and a 0.3 mm incident slit with a 2 mm mask; on the diffracted side, a 0.3 mm receiving slit and a 2.5° Soller slit were used. Data analysis was performed using SmartLab Studio II software. The lattice parameters of the film and substrate were determined with an accuracy of ± 0.0005 Å.

The optical properties of the film and substrate were investigated using variable-angle spectroscopic ellipsometry. Measurements were performed at room temperature on a J. A. Woollam VUV-VASE ellipsometer. The optical dielectric functions were extracted from the ellipsometric angle spectra using the commercial WVASE32 software package, and the optical absorption coefficient was calculated from these dielectric functions. Additional details on the ellipsometry measurements and data processing are provided elsewhere.[47,49,50] Previously obtained optical properties of single-crystal STO and of a thin strained STO film on LSAT were used as reference data for comparison.[39,48,50]

Results and discussion

Theoretical crystal and band structure

First-principles analysis of the local lattice distortions was performed for Mn substitution on the Ti site within the tetragonal model (SG 140) of STO. Compared to the TiO_6 octahedra in unstressed pure STO, the MnO_6 octahedra isotropically shrink, *i.e.* all interatomic distances lessen, in unstressed MSTO. The lattice parameters of MSTO diminish with respect to STO correspondingly. For ease of comparison, the lattice parameter a_P of a pseudo-cubic perovskite subcell was estimated as $a_P = [0.25(a_T \times b_T \times c_T)]^{1/3}$, where $a_T = b_T$ and c_T are the lattice parameters calculated in the tetragonal model. The lattice deformation associated with Mn(Ti) substitution is defined as $s_{Mn} = (a_{PMSTO}/a_{PSTO} - 1)$, where the perovskite cell parameters a_{PMSTO} and a_{PSTO} refer to MSTO and STO, respectively. The theoretical deformation is contraction on the order of 10^{-3} (Fig. 1(a)).

The revealed Mn(Ti)-induced lattice contraction is consistent with the lattice contraction induced by an LSAT substrate in cube-on-cube epitaxial STO films. In other words, the magnitude of the in-plane film-substrate lattice misfit decreases with increasing Mn content (Fig. 1(b)). Compared to the contractive lattice misfit −0.9% in epitaxial STO/LSAT films, the misfit is smaller in epitaxial MSTO/LSAT films, reaching only −0.3% at Mn content $x = 0.2$ (line substrate I in Fig. 1(b)). Notably, for a substrate that induces contractive misfit −0.4% in pure STO films, the misfit in MSTO becomes zero at Mn content 0.13 whereas it changes from contractive to dilative at higher Mn concentrations (line substrate II in Fig. 1(b)). Thus, contractive Mn(Ti) substitution is promoted when MSTO films are grown epitaxially on appropriately contractive substrates.

In contrast to the isotropic shrinkage of MnO_6 octahedra associated with Mn(Ti) substitution, Mn occupying the Sr site produces anisotropic local distortions: relative to the central position of Sr in STO, Mn(Sr) becomes off-centered. On the macroscopic scale, these local distortions translate into insignificant changes in the average lattice parameters. It is worth noting that a tendency toward lattice dilation for Mn(Sr) has been reported previously.[24] Therefore, in epitaxial films on contractive substrates, Mn(Sr) substitution is less favorable than contractive Mn(Ti) substitution.

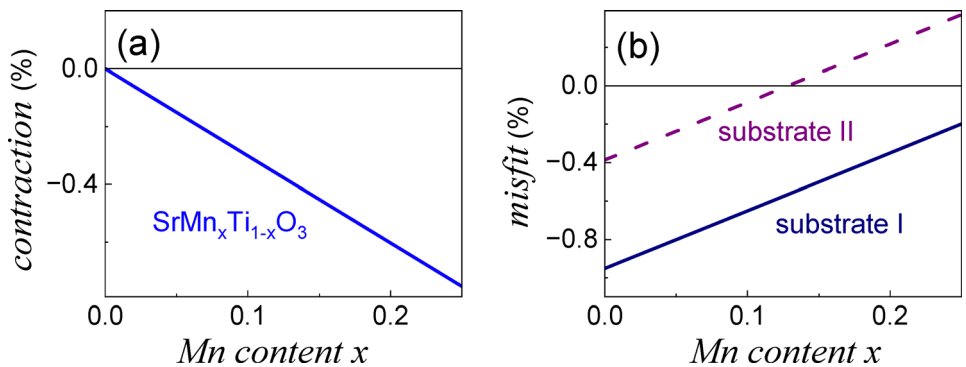

Fig. 1 (a) Interpolated theoretical Mn(Ti)-induced lattice contraction as a function of Mn content x in $SrTi_{1-x}Mn_xO_3$. (b) Theoretical film-substrate lattice misfit as a function of Mn content x in epitaxial $SrTi_{1-x}Mn_xO_3$ films on different substrates.

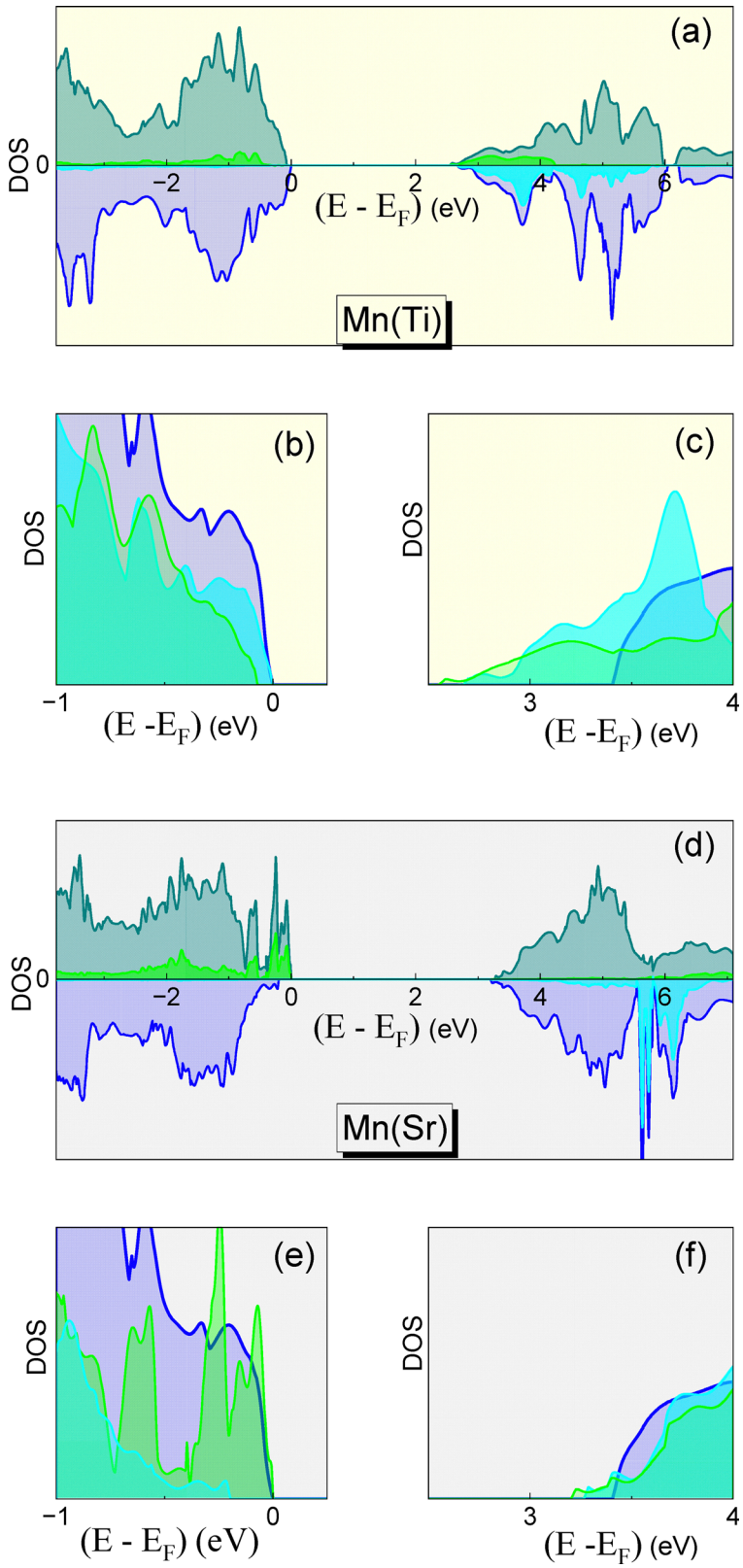

Fig. 2 Calculated DOS as a function of energy difference ($E - E_F$) from the Fermi level E_F for the (a)–(c) Mn(Ti) and (d)–(f) Mn(Sr) substitutions. In (a) and (d), green and cyan colours show partial Mn DOS for the α- and β- electrons, correspondingly. In (b), (c), (e) and (f), joint DOS for the α- electrons (green) and β- electrons (cyan) are shown together with that for pure STO (blue colour).

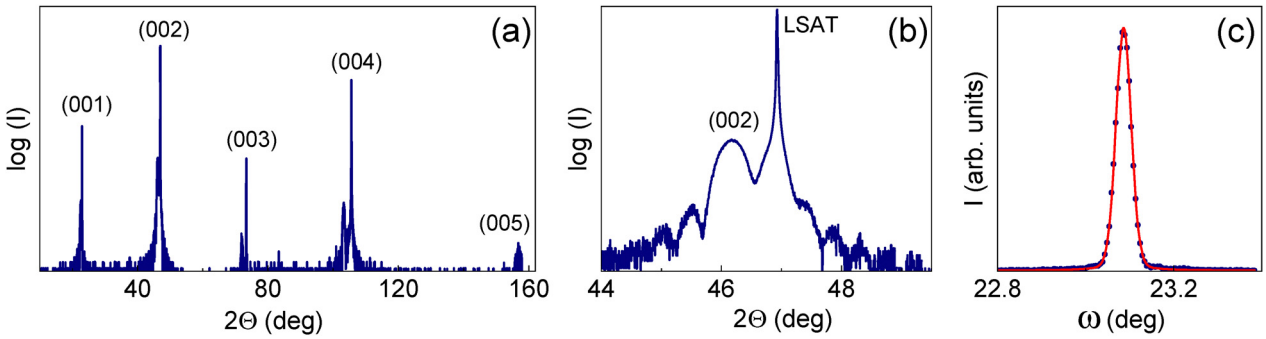

Fig. 3 HRXRD (a) and (b) $2\Theta-\omega$ scans. In (a), (00l) LSAT diffractions are marked. In (b), details around the (002) perovskite diffraction are shown (thickness 20.4 nm). (c) Rocking curve around the (001) perovskite diffraction. Solid curve shows pseudo-Voigt fit (FWHM 0.04 deg).

The obtained theoretical trends thus justify the dominant substitution of Mn on the Ti site in epitaxial MSTO films grown on LSAT.

The Mn substitution produces distinct modifications in the electronic band structure, which we track through calculations of the partial and joint density of states (DOS). In pure STO, the valence-band maximum (VBM) is predominantly formed by oxygen states, whereas the conduction-band minimum (CBM) is dominated by Ti states (SI Fig. S1).

As expected for Mn(Ti) substitution, replacing Ti with Mn primarily affects the CBM (Fig. 2(a)–(c)). For α-electrons with spin +1/2 and β-electrons with spin −1/2, the calculations reveal Mn(Ti)-derived states within the conduction band (Fig. 2(a)). The VBM remains essentially unchanged relative to pure STO (Fig. 2(b)), while the Mn(Ti) states introduce pronounced band tails at the CBM (Fig. 2(c)). The calculated bandgap of pure STO is 3.41 eV, and the Mn(Ti)-induced band tails extend approximately 0.8 eV into the STO gap (Fig. 2(c)). Notably, a strong additional Mn-related maximum appears at the CBM for β-electrons (Fig. 2(f)). The presence of such a well-defined anomaly in the DOS suggests the possibility of a specific Mn-related interband optical transition.

The influence of substrate-induced stress or strain on the DOS is negligible for both STO (SI Fig. S2) and MSTO (SI Fig. S3).

In contrast to the Mn(Ti)-induced modifications in the conduction band, the dominant contributions of the Mn(Sr) states appear at the VBM (Fig. 2(d)). Although Mn(Sr)-related states are also present deeper in the conduction band, they do not affect the CBM. Relative to STO, the band edges remain essentially unchanged upon Mn(Sr) substitution (Fig. 2(e) and (f)).

The theoretical rationale for Mn(Ti)-derived states near the CBM and Mn(Sr)-derived states near the VBM is expected to remain valid at lower Mn concentrations, whereas the calculated extent of in-gap tailing (Fig. 2(c)) should be regarded only as an approximate indicator.[52–54]

The theoretical results in Fig. 2 signify that Mn(Ti) substitution should manifest in distinct optical signatures: the near-edge optical absorption is expected to exhibit a pronounced in-gap tail and the emergence of additional Mn-related optical transition(s). Contrarily, Mn(Sr) substitution should not affect the near-edge optical absorption.

Optical properties in thin film

To experimentally verify the theoretical DOS predictions, we prepared a high-quality epitaxial MSTO film on a (001) LSAT substrate and investigated its optical properties in detail. Compared to the STO/LSAT misfit strain, Mn(Ti) substitution reduces—but does not eliminate—the film-substrate misfit in epitaxial MSTO/LSAT films at Mn content 0.02. The presence of non-zero lattice misfit typically leads to strain relaxation with increasing film thickness. The resulting inhomogeneous strain, *i.e.*, a depth-dependent strain distribution, is known to produce band tailing and to smear the optical absorption edge.[39,41] These effects can obscure the intrinsic optical signatures predicted for Mn(Ti) substitution and hinder identification of the Mn-related contributions. To avoid (or significantly suppress) inhomogeneous strain, the nominal thickness of the MSTO/LSAT film was limited to only 20 nm.

HRXRD analysis shows that the crystal structure of the thin MSTO/LSAT film can be described as pseudo-cubic perovskite, with the (00l) planes parallel to those of the substrate (Fig. 3(a)). Reciprocal-space maps (SI Fig. S4) reveal an in-plane cube-on-cube epitaxial relationship, with the [100] directions of the MSTO film aligned with those of the substrate. The film's high crystalline quality is evidenced by the presence of Pendellösung diffraction satellites (Fig. 3(b)). The coherence-length thickness estimated from the satellite positions is 20.4 nm, in agreement with the nominal film thickness, confirming the fully epitaxial character of the film. Finally, the measured rocking curve (Fig. 3(c)) is very narrow, further corroborating the film's crystalline perfection.

The in-plane and out-of-plane lattice parameters extracted from the maxima in the reciprocal-space maps are 3.890 Å and 3.927 Å, respectively. The in-plane parameter of the film is slightly larger than that of LSAT (3.871 Å), indicating minor relaxation of the misfit strain.

We note that, in addition to the XRD-based estimation of the coherent film thickness, the film thickness was also independently assessed using spectroscopic ellipsometry. The optically determined thickness is (20.37 ± 2.55) nm, in agreement with both the nominal thickness and the XRD-derived value. This consistency strongly supports the high crystalline quality of the film.

The optical properties of the thin, high-quality MSTO film were analyzed in comparison with those of a reference STO single crystal (SI Note S3). The experimental absorption spectrum

of the MSTO film differs markedly from that of STO (Fig. 4(a)). While the onset of fundamental absorption occurs at ~3.9 eV and the main broad peak appears near ~5 eV in both MSTO and STO, the near-edge in-gap absorption coefficient is significantly larger in MSTO, and the peak at ~6.5 eV is blue-shifted relative to STO.

The Tauc plots[55–62] for direct bandgaps, $(\alpha E)^2 \propto (E - E_D)$, where α and E_D are the absorption coefficient and direct bandgap, respectively, are shown in Fig. 4(b). The good linear fits indicate the presence of direct interband transitions in both MSTO and STO. The fitted direct gap is $E_D = (3.82 \pm 0.02)$ eV in MSTO, close to the reference value of $E_D = (3.86 \pm 0.02)$ eV in STO crystal.

The Tauc plots for indirect bandgaps, $(\alpha E)^{1/2} \propto (E - E_I)$, reveal an indirect bandgap of $E_I = (3.25 \pm 0.02)$ eV in STO, but cannot show an indirect bandgap in MSTO (Fig. 4(c)). In addition to the lack of evidence for an indirect transition, pronounced absorption is observed below the direct bandgap at $E < 3.8$ eV in MSTO. The semi-logarithmic plot in Fig. 4(d) exhibits a clear linear dependence, $\log(\alpha) \propto E$, for $E < 3$ eV, characteristic of an Urbach-type absorption tail: $\alpha = \alpha_0 \exp(E/E_U)$, where the Urbach energy E_U

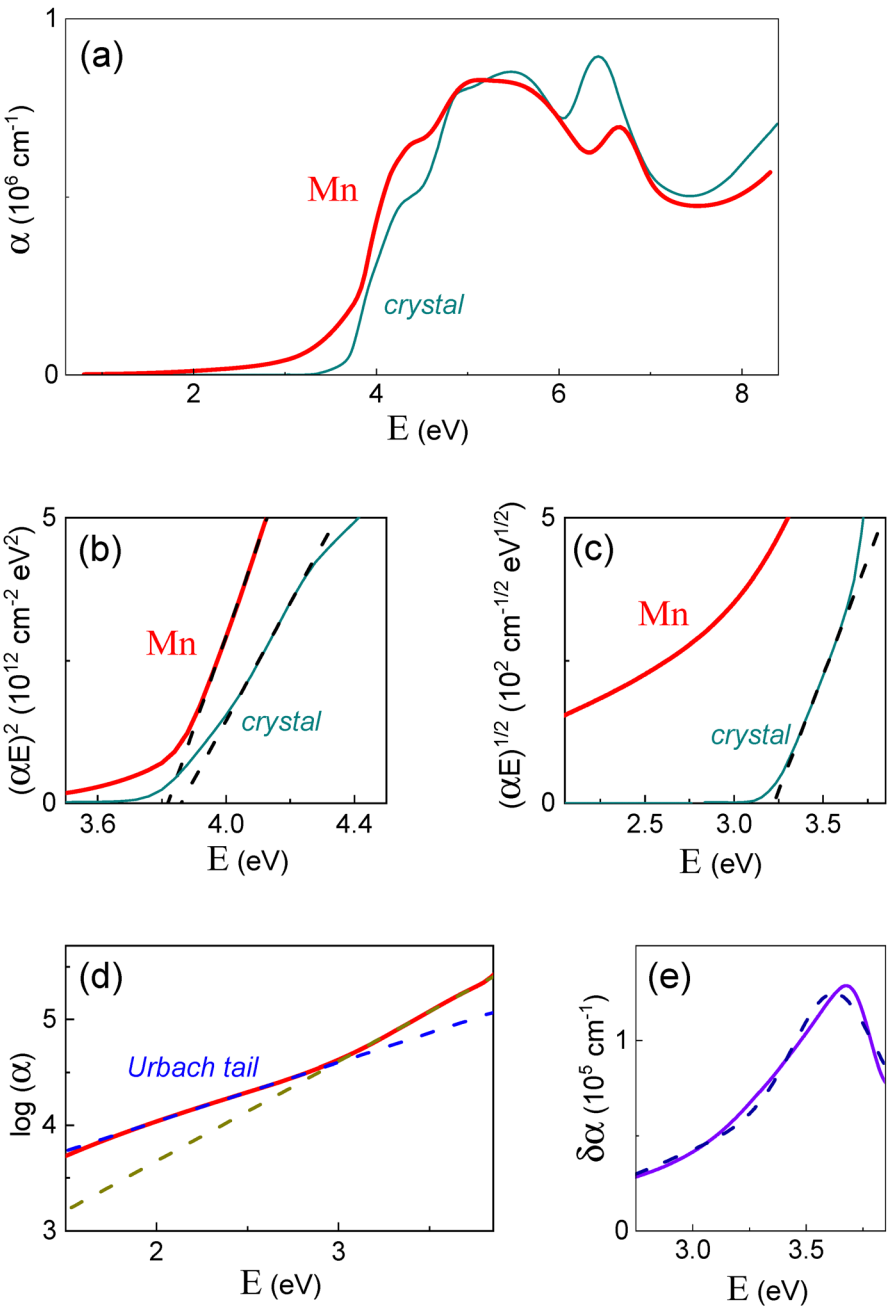

Fig. 4 (a) Absorption coefficient as a function of photon energy and (b) and (c) Tauc plots with linear fits (dashed lines) for (b) direct and (c) indirect gaps. Thin curves show reference STO crystal data in (a)–(c). (d) Urbach plot with linear fits (dashed lines). (e) Near-edge additional absorption compared to crystal. Dashed curve shows pseudo-Voigt fit.

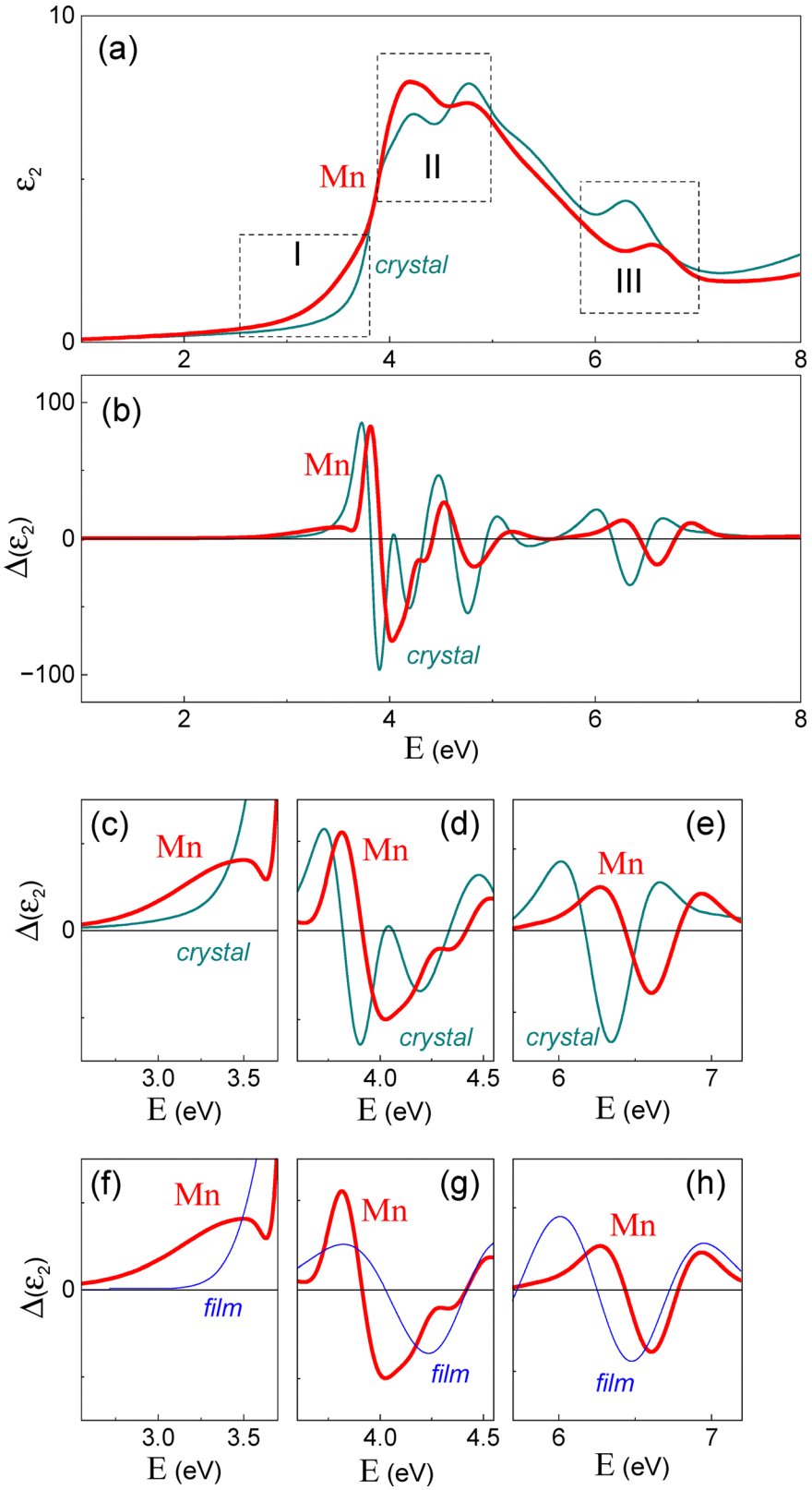

Fig. 5 (a) Imaginary part of the dielectric function and (b)–(h) its second derivative as a function of photon energy. Thin curves show reference data for (c)–(e) STO crystal and (f)–(h) STO/LSAT film.

describes the in-gap tail depth.[63–71] The fitted Urbach energy is E_U = (0.78± 0.01) eV. This experimentally determined tail is consistent with the theoretically predicted in-gap extension of the DOS at the CBM in MSTO (Fig. 2(c)).

We note that for photon energies between 3 and 3.8 eV, a second linear segment with a smaller E_U can be formally extracted from the log (α) plot. However, the absorption magnitude in this range is large, on the order of 10^5 cm^{-1}, indicating that this feature arises from an interband transition rather than from band tailing. Interestingly, the difference in absorption coefficients between MSTO and STO, $\delta\alpha$, exhibits a maximum near ∼3.6 eV (Fig. 4(e)), suggesting the presence of an additional optical transition in MSTO that is absent in STO.

To examine the interband transitions in greater detail, we analyzed the complex dielectric function and its second derivative (Fig. 5 and SI Fig. S5, SI Note S4). This approach reveals additional Mn-related effects. Three spectral regions of the dielectric function show clear differences between MSTO and STO (Fig. 5(a)). Compared to STO, the imaginary part of the dielectric function, ε_2, in MSTO is enhanced at $E < 3.8$ eV (region I), redistributed around $E \approx 5$ eV (region II), and blue-shifted at $E > 6$ eV (region III). The second derivative $\Delta(\varepsilon_2) = d^2\varepsilon_2/dE^2$ (Fig. 5(b)) highlights these differences in terms of critical points (CPs) in the DOS and the interband (or intraband) transitions associated with them (SI Note S4).

In spectral region I, a Mn-related CP near ∼3.5 eV is observed in MSTO (Fig. 5(c)). We attribute this feature to the theoretically predicted anomaly at 3.5 eV in the DOS (Fig. 2(c)).

In spectral region II, the main STO feature at ∼4 eV appears smeared in MSTO (Fig. 5(d)), and the STO CP at ∼4.6 eV is strongly suppressed in MSTO (Fig. 5(b)). Finally, in spectral region III, the CP at energies above 6 eV exhibits a pronounced blue shift: the CP energy is ∼6.6 eV in MSTO compared to ∼6.3 eV in STO.

It is worth noting that, relative to the reference unstressed cubic STO crystal, the MSTO/LSAT film exhibits a metrically tetragonal crystal structure and experiences anisotropic lattice strain. To confirm that the additional CP (3.5 eV), the smeared CP (4 eV), and the blue-shifted CP (6.6 eV) arise from Mn(Ti) substitution rather than from lattice symmetry or strain, we compared the derivative $\Delta(\varepsilon_2)$ of the MSTO/LSAT film with that of a strained pure STO/LSAT film reported previously.[48] As shown in Fig. 5(f)–(h), the CP features in question are present in the MSTO film but absent in the strained STO film. These results confirm that Mn(Ti) substitution is responsible for the revealed optical effects.

The experimentally observed intrinsic effects of Mn(Ti) substitution on the optical properties of STO include: band tailing with an in-gap depth of ∼0.8 eV, an additional near-edge transition, smearing of the main direct transition near 4 eV, and a blue-shifted transition above 6 eV. The near-edge features agree well with the theoretically calculated DOS, which shows Mn(Ti)-related tails and additional maxima/minima at the bottom of the conduction band. The in-gap conduction-band tailing is substantial.

We emphasize that in DOS calculations, such in-gap tails are often interpreted as bandgap narrowing. However, DOS calculations do not account for the quantum efficiency of electronic transitions, and therefore the theoretical bandgap extracted from DOS does not necessarily correspond to the experimental optical bandgap. Here, the experimental and theoretical results are considered together. The key finding is that Mn(Ti) substitution induces pronounced tailing of the conduction band in STO.

Conclusions

The combined theoretical and experimental investigations establish the impact of Mn substitution for Ti on the electronic structure of STO. First-principles calculations show that Mn(Ti) incorporation induces lattice contraction and introduces distinct modifications to the conduction-band DOS, including pronounced band tailing and additional fine structure. To validate these predictions, a high-quality epitaxial Mn-doped STO film was grown on a contractive LSAT substrate that promotes contractive Mn substitution on the Ti site. The optical properties of the film, benchmarked against crystal and epitaxial STO, reveal a consistent set of Mn-induced features: a deep 0.8 eV in-gap tail, emergence of a near-edge transition, smearing of the main direct transition near 4 eV, and a blue-shifted transition above 6 eV. The strong correspondence between calculated and measured signatures provides compelling evidence that Mn(Ti) substitution drives conduction-band tailing in STO.

Author contributions

M. T.: conceptualization; methodology; formal analysis; funding acquisition; supervision; writing – original draft; writing – review & editing. L. R.: investigation; writing – original draft. E. P.: investigation; writing – original draft. N. N.: investigation. T. K.: investigation. E. K.: methodology; funding acquisition. A. D.: methodology; funding acquisition.

Conflicts of interest

There are no conflicts to declare.

Data availability

Data for this article, including ellipsometry data are available at Zenodo https://doi.org/10.5281/zenodo.21625114.

Supplementary information (SI) is available. See DOI: 10.1039/d6ma00825a.

Acknowledgements

The authors acknowledge support from the Czech Academy of Sciences through the program Strategy AV21''Breakthrough technologies for the future – sensing, digitization, artificial intelligence, and quantum technologies'' and M-ERA.NET project GRIPHUS (project 12471).

References

1 K. A. Müller, *Phys. Rev. Lett.*, 1959, **2**, 341–343.

2 R. A. Serway, W. Berlinger, K. A. Müller and R. W. Collins, *Phys. Rev. B*, 1977, **16**, 4761–4768.
3 K. W. Blazey, J. M. Cabrera and K. A. Müller, *Solid State Commun.*, 1983, **45**, 903–906.
4 C. B. Azzoni, M. C. Mozzati, A. Paleari, V. Massarotti, M. Bini and D. Capsoni, *Solid State Commun.*, 2000, **114**, 617–622.
5 A. Tkach, P. M. Vilarinho and A. L. Kholkin, *Appl. Phys. Lett.*, 2005, **86**, 172902.
6 A. Tkach, P. M. Vilarinho and A. L. Kholkin, *Acta Mater.*, 2006, **54**, 5385–5391.
7 A. Tkach, P. M. Vilarinho, A. L. Kholkin, A. Pashkin, S. Veljko and J. Petzelt, *Phys. Rev. B: Condens. Matter Mater. Phys.*, 2006, **73**, 104113.
8 V. A. Trepakov, M. Savinov, V. Železný, J. Pokorný, P. Syrnikov, C. B. Azzoni, P. Galinetto, M. C. Mozzati, A. Badalyan, A. Deyneka and L. Jastrabik, *J. Phys.: Conf. Ser.*, 2007, **93**, 012017.
9 M. Savinov, V. A. Trepakov, P. P. Syrnikov, V. Zelezny, J. Pokorny, A. Dejneka, L. Jastrabik and P. Galinetto, *J. Phys.: Condens. Matter*, 2008, **20**, 095221.
10 A. I. Lebedeva, I. A. Sluchinskaya, A. Erko and V. F. Kozlovskii, *JETP Lett.*, 2009, **89**, 457–460.
11 I. A. Sluchinskaya, A. I. Lebedev and A. Erko, *Bull. Russ. Acad. Sci.: Phys.*, 2010, **74**, 1235–1237.
12 D. Choudhury, S. Mukherjee, P. Mandal, A. Sundaresan, U. V. Waghmare, S. Bhattacharjee, R. Mathieu, P. Lazor, O. Eriksson, B. Sanyal, P. Nordblad, A. Sharma, S. V. Bhat, O. Karis and D. D. Sarma, *Phys. Rev. B: Condens. Matter Mater. Phys.*, 2011, **84**, 125124.
13 M. Valant, T. Kolodiazhnyi, I. Arcon, F. Aguesse, A.-K. Axelsson and N. M. Alford, *Adv. Funct. Mater.*, 2012, **22**, 2114–2122.
14 D. V. Azamat, A. G. Badalyan, A. Dejneka, V. A. Trepakov, L. Jastrabik and Z. Frait, *J. Phys. Chem. Solids*, 2012, **73**, 822–826.
15 J. Kubacki, D. Kajewski, A. Koehl, M. Wojtyniak, R. Dittmann and J. Szade, *Radiat. Phys. Chem.*, 2013, **93**, 123–128.
16 J. A. Dawson, H. Chen and I. Tanaka, *J. Phys. Chem. C*, 2014, **118**, 14485–14494.
17 H. Yang, P. G. Kotula, Y. Sato, M. Chi, Y. Ikuharac and N. D. Browning, *Mater. Res. Lett.*, 2014, **2**, 16–22.
18 V. Trepakov, M. Makarova, O. Stupakov, E. A. Tereshina, J. Drahokoupil, M. Cernanský, Z. Potucek, F. Borodavka, V. Valvoda, A. Lynnyk, A. Jäger, L. Jastrabik and A. Dejneka, *Mater. Chem. Phys.*, 2014, **143**, 570–577.
19 T. D. Thanh, T. L. Phan, L. M. Oanh, N. V. Minh, J. S. Lee and S. C. Yu, *IEEE Trans. Magn.*, 2014, **50**, 1–4.
20 A. Zorko, M. Pregelj, H. Luetkens, A. K. Axelsson and M. Valant, *Phys. Rev. B:Condens. Matter Mater. Phys.*, 2014, **89**, 094418.
21 R. A. Maier, A. C. Johnston-Peck and M. P. Donohue, *Adv. Funct. Mater.*, 2016, **26**, 8325–8333.
22 H. Mansoor, W. L. Harrigan, K. A. Lehuta and K. R. Kittilstved, *Front. Chem.*, 2019, **7**, 353.
23 R. A. Maier, E. Cockayne, M. Donohue, G. Cibin and I. Levin, *Chem. Mater.*, 2020, **32**, 4651–4662.
24 G. M. Repa and L. A. Fredin, *Appl. Phys. Lett.*, 2022, **121**, 022401.
25 M. V. Talanov, A. I. Stash, S. A. Ivanov, E. S. Zhukova, B. P. Gorshunov, B. M. Nekrasov, A. V. Melentev, V. I. Kozlov, V. M. Cherepanov, S. Y. Gavrilkin, A. Y. Tsvetkov, I. A. Zavidovskiy, M. K. Tatmyshevskiy, M. Savinov, V. M. Talanov and A. A. Bush, *J. Mater. Chem. C*, 2024, **12**, 8105–8118.
26 S. Pandey, A. Agrawal and S. Dubey, *J. Alloys Compd.*, 2025, **1040**, 183540.
27 F. T. Wagner and G. A. Somorjai, *Nature*, 1980, **285**, 559.
28 H. C. Chen, C. W. Huang, J. C. S. Wu and S. T. Lin, *J. Phys. Chem. C*, 2012, **116**, 7897.
29 E. García-López, G. Marcì, B. Megna, F. Parisi, L. Armelao, A. Trovarelli, M. Boaro and L. Palmisano, *J. Catal.*, 2015, **321**, 13.
30 S. Patial, V. Hasija, P. Raizada, P. Singh, A. A. P. K. Singh and A. M. Asiri, *J. Environ. Chem. Eng.*, 2020, **8**, 103791.
31 B. Moss, Q. Wang, K. T. Butler, R. Grau-Crespo, S. Selim, A. Regoutz, T. Hisatomi, R. Godin, D. J. Payne, A. Kafizas, K. Domen, L. Steier and J. R. Durrant, *Nat. Mater.*, 2021, **20**, 511.
32 Y. S. Hou, S. Ardo and R. Q. Wu, *Phys. Rev. Mater.*, 2021, **5**, 065801.
33 R. Joy and S. Haridas, *Int. J. Hydrogen Energy*, 2021, **46**, 1879.
34 Y. Yoshiyama, S. Hosokawa, H. Asakura, K. Teramura and T. Tanaka, *J. Phys. Chem. C*, 2022, **126**, 4415.
35 A. Viernstein, M. Kubicek, M. Morgenbesser, T. M. Huber, M. Siebenhofer and J. Fleig, *Mater. Adv.*, 2022, **3**, 2800.
36 C. Avcıoğlu, S. Avcıoğlu and M. F. Bekheet, *ACS Appl. Energy Mater.*, 2023, **6**, 1134.
37 C. Courter, J. Stewart and T. Cuk, *J. Phys. Chem. C*, 2023, **127**, 4905.
38 D. A. Freedman, D. Roundy and T. A. Arias, *Phys. Rev. B: Condens. Matter Mater. Phys.*, 2009, **80**, 064108.
39 M. Tyunina, N. Nepomniashchaia, O. Pacherova, T. Kocourek, V. Vetokhina and A. Dejneka, *Mater. Adv.*, 2025, **6**, 6575.
40 M. Tyunina, M. Savinov, O. Pacherova, T. Kocourek, P. Yudin and A. Dejneka, *APL Mater.*, 2025, **13**, 031101.
41 V. Vetokhina, N. Nepomniashchaia, E. de Prado, O. Pacherova, T. Kocourek, S. S. Anandakrishnan, Y. Bai, A. Dejneka and M. Tyunina, *Mater. Adv.*, 2024, **5**, 8901.
42 A. Erba, J. K. Desmarais, S. Casassa, B. Civalleri, L. Donà, I. J. Bush, B. Searle, L. Maschio, L. Edith-Daga and A. Cossard, *et al.*, *J. Chem. Theory Comput.*, 2023, **19**, 6891–6932.
43 R. Dovesi, V. R. Saunders, C. Roetti, R. Orlando, C. M. Zicovich-Wilson, F. Pascale, B. Civalleri, K. Doll, N. M. Harrison and I. J. Bush, *et al.*, *CRYSTAL23 User's Manual*, University of Torino: Torino, Italy, 2022.
44 S. Piskunov, E. Heifets, R. I. Eglitis. and G. Borstel, *Comput. Mater. Sci.*, 2004, **29**, 165.
45 M. F. Peintinger, D. Vilela Oliveira and T. Bredow, *J. Comput. Chem.*, 2012, **34**, 451–459.
46 L. L. Rusevich, M. Tyunina, E. A. Kotomin, N. Nepomniashchaia and A. Dejneka, *Sci. Rep.*, 2021, **11**, 23341.
47 L. L. Rusevich, E. A. Kotomin, G. Zvejnieks, M. M. Kržmanc, S. Gupta, N. Daneu, J. C. S. Wu, Y.-G. Lee and W.-Y. Yu, *J. Phys. Chem. C*, 2022, **126**, 21223–21233.
48 M. Tyunina, N. Nepomniashchaia, V. Vetokhina and A. Dejneka, *Appl. Phys. Lett.*, 2020, **117**, 082901.

49 M. Tyunina, L. L. Rusevich, E. A. Kotomin, O. Pacherova, T. Kocourek and A. Dejneka, *J. Mater. Chem. C*, 2021, **9**, 1693.
50 M. Tyunina, N. Nepomniashchaia, V. Vetokhina and A. Dejneka, *APL Mater.*, 2021, **9**, 121108.
51 N. Nepomniashchaia, O. Pacherova, T. Kocourek, A. Dejneka and M. Tyunina, *J. Appl. Phys.*, 2025, **137**, 014103.
52 J. Carrasco, F. Illas, N. Lopez, E. A. Kotomin, Yu. F. Zhukovskii, R. A. Evarestov, Yu. A. Mastrikov, S. Piskunov and J. Maier, *Phys. Rev. B:Condens. Matter Mater. Phys.*, 2006, **73**, 064106.
53 R. A. Evarestov, E. A. Kotomin and Yu. F. Zhukovskii, *Int. J. Quantum Chem.*, 2006, **106**, 2173.
54 Y. F. Zhukovskii, E. A. Kotomin, R. A. Evarestov and D. E. Ellis, *Int. J. Quantum Chem.*, 2007, **107**, 2956.
55 R. J. Elliott, *Phys. Rev.*, 1957, **108**, 1384.
56 J. Tauc, R. Grigorovic and A. Vancu, *Phys. Status Solidi B*, 1966, **15**, 627.
57 M. Fox, *Optical Properties of Solids*, Oxford University Press, 2001.
58 M. Grundmann, *Semiconductor Physics: An Introduction Including Device and Nanophysics*, Springer, 2005.
59 B. D. Viezbicke, S. Patel, B. E. Davis and D. P. Birnie, *Phys. Status Solidi B*, 2015, **252**, 1700.
60 J. Klein, L. Kampermann, B. Mockenhaupt, M. Behrens, J. Strunk and G. Bacher, *Adv. Funct. Mater.*, 2023, **33**, 2304523.
61 M. L. Cohen and J. R. Chelikowsky, *Electronic Structure and Optical Properties of Semiconductors*, Springer, 1989.
62 P. Yu and M. Cardona, *Fundamentals of Semiconductors*, Springer, 1996.
63 F. Urbach, *Phys. Rev.*, 1953, **92**, 1324.
64 H. W. Martienssen, *J. Phys. Chem. Solids*, 1957, **2**, 257.
65 M. V. Kurik, *Phys. Status Solidi A*, 1971, **8**, 9.
66 J. D. Dow and D. Redfield, *Phys. Rev. B*, 1972, **5**, 594.
67 C. M. Soukoulis, M. H. Cohen and E. N. Economou, *Phys. Rev. Lett.*, 1984, **53**, 616.
68 S. John, C. Soukoulis, M. H. Cohen and E. N. Economou, *Phys. Rev. Lett.*, 1986, **57**, 1777.
69 G. D. Cody, *J. Noncryst. Solids*, 1992, **141**, 3.
70 P. V. Mieghem, *Rev. Mod. Phys.*, 1992, **64**, 755.
71 I. Studenyak, Ml Kranjčec and M. Kurik, *Int. J. Opt. Appl.*, 2014, **4**, 76.